ULUSLARARASI 3B YAZICI TEKNOLOJİLERİ
VE DİJİTAL ENDÜSTRİ DERGİSİ

INTERNATIONAL JOURNAL OF 3D PRINTING
TECHNOLOGIES AND DIGITAL INDUSTRY

ISSN:2602-3350 (Online)

URL: https://dergipark.org.tr/ij3dptdi

INFLUENCE OF ELECTROPHORETIC DEPOSITION ROUTES ON STRUCTURAL EVOLUTION AND ELECTRICAL BEHAVIOR OF ZNO COATING DEPOSITED ON WAAM INCONEL 625

Yazarlar (Authors): Doruk Gürkan*

Bu makaleye şu şekilde atıfta bulunabilirsiniz (To cite to this article): *Gürkan D., "Influence of Electrophoretic Deposition Routes on Structural Evolution and Electrical Behavior of ZnO Coating Deposited on WAAM Inconel 625" Int. J. of 3D Printing Tech. Dig. Ind., 10(1): 210-224, (2026).*

DOI: 10.46519/ij3dptdi.1901493

Araştırma Makale/ Research Article

Erişim Linki: (To link to this article): https://dergipark.org.tr/en/pub/ij3dptdi/archive

INFLUENCE OF ELECTROPHORETIC DEPOSITION ROUTES ON STRUCTURAL EVOLUTION AND ELECTRICAL BEHAVIOR OF ZNO COATING DEPOSITED ON WAAM INCONEL 625

Doruk Gürkan[a]*

[a]Istanbul Gedik University, Engineering Faculty, Mechanical Engineering Department, TÜRKİYE

* *Corresponding Author: dorukgrkan@yahoo.com*

(**Received:** 02.03.26; **Revised:** 17.03.26; **Accepted:** 15.04.26)

ABSTRACT

Wire Arc Additive Manufacturing (WAAM) surfaces exhibit heterogeneous microstructures and oxide layers which might influence coating deposition and interfacial properties. The influence of electrophoretic deposition chemistry on coating structure, coating architecture, and electrical properties of WAAM-fabricated nickel-based superalloys still lacks sufficient understanding. In this study, conventional electrophoretic deposition (EPD) and sol-gel derived electrophoretic deposition techniques were employed for ZnO coating deposition on WAAM-fabricated Inconel 625 superalloys. ZnO coatings were deposited at 10 V for 1 min and then subjected to heat treatment at 600°C for 1 h. The structural and morphological properties of ZnO coatings were studied using X-ray diffraction, scanning electron microscopy and energy-dispersive X-ray spectroscopy while the electrical properties were studied using a Wheatstone bridge circuit. The crystalline nature of ZnO coatings was observed for both conventional and sol-gel derived EPD routes; however, differences in coating structure and compactness were observed. Conventional EPD route exhibited a coating porosity of 14.2 ± 1.5% and coating thickness of 1.4 ± 0.2 µm while sol-gel derived EPD route exhibited a coating porosity of 3.8 ± 0.6% and coating thickness of 0.92 ± 0.18 µm. The Zn/(Ni + Cr) ratio was observed to increase from 0.62 to 3.23, indicating better coating coverage for sol-gel derived EPD route coatings. The conductivity of Inconel 625 was observed to reduce by 10.5% for conventional electrophoretic deposition route coatings and 7.2% for sol-gel electrophoretic deposition route coatings. The suspension chemistry was observed to influence coating compactness, coating structure and interfacial electrical properties of WAAM-fabricated Inconel 625 superalloys. Sol-gel derived EPD route coatings exhibited better homogeneity and electrical stability for ZnO coatings.

Keywords: WAAM, Inconel 625, ZnO coating, Electrophoretic deposition, Electrical conductivity.

1. INTRODUCTION

Wire Arc Additive Manufacturing (WAAM) has gained significant attention as a high-deposition-rate, cost-efficient metal additive manufacturing technique capable of producing large-scale structural components with complex geometries [1]. Nickel-based superalloys, particularly Inconel 625, are widely processed via WAAM due to their excellent mechanical strength, corrosion resistance and stability at elevated temperatures [2]. However, WAAM-fabricated surfaces inherently exhibit layer-wise solidification features, anisotropic grain structures, surface waviness, oxide inclusions and microstructural heterogeneity, all of which may influence surface-dependent functional properties such as corrosion resistance, interfacial charge transfer and electrical behavior [3].

Surface modification strategies are therefore essential to enhance or tailor the functional performance of WAAM-produced components. Among functional oxide materials, zinc oxide (ZnO) has attracted extensive research interest due to its wide band gap (~3.37 eV), high exciton binding energy (~60 meV), chemical stability and tunable electrical conductivity [4]. ZnO exhibits semiconducting behavior that can be modulated through intrinsic defects or dopant incorporation, making it suitable for sensing, photocatalytic, optoelectronic and

corrosion-protective applications [5-6]. Importantly, ZnO-based coatings can influence charge transport mechanisms and interfacial electrical resistance when deposited on conductive metallic substrates.

Electrophoretic deposition (EPD) is a versatile approach for scaling up the deposition of ceramic particles onto conductive surfaces using an electric field [7]. It has been commended for its simplicity, control of film thickness, lower equipment requirements and applicability to complex geometries [8]. In electrophoretic deposition, powder particles dispersed in a liquid migrate to the electrode under the electric field and accumulate in a deposition-controlled manner. However, problems such as particle aggregation, porosity and cracks have been encountered during the drying process [9].

In order to mitigate the drawbacks associated with the methods, researchers are opting for the sol-gel-derived EPD technique. In situ hydrolysis and polycondensation reactions are employed which help in the effective bonding between the particles during the deposition process as well as the subsequent heat treatment [10]. In comparison to the powder-based suspension, the sol-gel-derived process provides better stability, controlled nucleation, minimized agglomeration and densification of the film, as presented in Table 1 [11-12]. These properties are particularly important in the case of thin films where the compactness, defect density and smoothness of the interface are significant parameters in the effective conduction of electricity and the insulation of the substrate.

Table 1. Expected Comparison of ZnO deposition mechanisms on WAAM-produced Inconel 625

Mechanistic Parameter	EPD	Sol–Gel Derived EPD
Deposition unit	Discrete ZnO particles	Molecular/complexed Zn species
Response to surface roughness	Field-driven clustering	Gradual infiltration and condensation
Sensitivity to microsegregation	High	Lower
Interfacial interaction	Predominantly mechanical	Possible chemical coordination
Film formation mode	Particle stacking	Condensation-assisted network formation
Expected film compactness	Moderate, agglomeration-prone	Higher, improved connectivity

Although ZnO coatings and EPD processing have been extensively investigated in various contexts, studies specifically focusing on ZnO deposition onto WAAM-fabricated Inconel 625 substrates remain limited. More importantly, the comparative influence of EPD and sol–gel derived EPD routes on coating architecture, substrate signal attenuation and electrical resistance behavior has not been systematically clarified. Given that WAAM surfaces present unique topographical and metallurgical characteristics, deposition chemistry may play a decisive role in determining coating compactness and functional response [13].

Therefore, the present study aims to comparatively evaluate conventional EPD and sol–gel derived EPD routes for ZnO coating deposition on WAAM-fabricated Inconel 625. The coatings are systematically characterized in terms of phase composition (XRD), surface and cross-sectional morphology (SEM), elemental distribution (EDS) and electrical resistance behavior. Particular emphasis is placed on correlating deposition chemistry with film densification, substrate shielding efficiency and electrical transport characteristics.

2. MATERIAL AND METHOD

WAAM-fabricated substrates were produced using a system operating under controlled deposition parameters. A commercially available Inconel 625 welding wire (diameter: 1.2 mm, composition in accordance with ASTM B443-GeKa Addwire Inconel 625,Türkiye) was employed as feedstock material. The nominal composition of the alloy by weight consists mainly of nickel with the rest being other elements, chromium 20–23%, molybdenum 8–10% and niobium 3–4%, with iron and trace elements. These compositional values are based on the supplier's datasheet. The welding process was done using a gas metal arc welding (GMAW) setup. The welding parameters were adjusted to maintain stability of the arc and symmetry of the bead. The welding was done

with 160 A of current, 22 V of voltage and 15 mm/s of speed. Argon (99.99% purity) 2.5% O_2 gas mixture was used as shielding gas at a flow rate of 15 L/min to minimize oxidation during deposition.

Layer-by-layer deposition was performed to obtain rectangular wall structures with approximate dimensions of 150 × 400 × 12 mm. Interpass temperature was monitored and controlled below 400 °C to reduce excessive heat accumulation and minimize residual stress development. After fabrication, the samples were allowed to cool naturally to room temperature under ambient conditions.

WAAM-fabricated walls were sectioned into rectangular specimens (15 × 25 × 2 mm) using abrasive waterjet cutting in order to avoid thermal distortion and microstructural alteration associated with conventional machining techniques [14]. Electrophoretic deposition experiments were performed on the cut cross-sectional surfaces of the specimens. Samples were lightly ground using 400 and 800 grit SiC papers to remove loosely adhered surface irregularities while preserving the characteristic WAAM surface morphology. The samples were ultrasonically cleaned in ethanol and pure water, respectively for 10 min and dried in air.

To evaluate the suitability of sol–gel-derived systems for electrophoretic deposition, two different ZnO-based suspensions were prepared and comparatively investigated: (i) a conventional EPD formulation and (ii) a modified sol–gel solution tailored for EPD compatibility. The suspensions were comparatively assessed in terms of colloidal stability, electrical conductivity and deposition behavior under an externally applied electric field. WAAM-fabricated Inconel 625 specimens were used as both working and counter electrodes. The inter-electrode distance was fixed at 20 mm. Prior to deposition, surface activation was performed to remove passive oxide layers and enhance surface reactivity. For this purpose, the electrodes were immersed in 1 M NaOH solution and subjected to 1.5 V for 60 s.

EPD system consisted of a DC power supply (Twintex SP-6005, Twintex Instrument Ltd., Taiwan) and a magnetic stirring unit (Heidolph MR 3001K, Heidolph Scientific Products GmbH, Germany). Deposition was completed under a constant 10V voltage for 1 minute. Throughout the process, the current was continuously monitored to maintain stability and detect abnormal current variations to observe suspension instability and gas release within the solution. The deposition current was maintained between 50mA for both electrophoretic deposition routes.

The pH of the aqueous suspensions was determined by using an Ohaus Starter300 pH meter (Ohaus Europe GmbH, Switzerland). The pH value of the suspensions played a vital role in the electrophoretic mobility and electrophoretic deposition of ZnO suspensions. In the case of aqueous suspensions for electrophoretic deposition, pH should be between 8 and 9 which ZnO particles are negatively charged and show stable colloidal dispersion and anodic electrophoresis under the influence of an electric field [15-16]. If pH of the suspension drops below 7, ZnO particles dissolve to Zn^{+2} ions and precipitate, resulting in poor coating quality. Hence, it is important to maintain the pH within this range for stable suspensions and uniform coating growth. Diethanolamine (DEA) was used as pH stabilizer. The precursor solution was analytical grade zinc acetate dihydrate (Merck) which was added to 2.2g/100ml and mixed with 50/50vol.% ethanol and distilled water. EPD mixtures were magnetically stirred for 60 min-250 rpm, followed by ultrasonication for 60 min to break down agglomerates and ensure homogeneous dispersion. The stability of the suspension was visually monitored and used immediately after preparation to prevent sedimentation effects.

For the modified sol–gel system but dissolved in a mixed solvent consisting of ethanol and distilled water (50/50 vol.%). Diethanolamine (DEA) was added as a stabilizing and complexing agent to control hydrolysis and condensation reactions of the zinc precursor

In alcohol-based sol–gel suspension, ethanol was used as the solvent while the precursor concentration was maintained the same as in conventional EPD suspension. Conventional pH measurement becomes less reliable due to the reduced activity of H^+ and OH^- ions in non-aqueous media [17]. Consequently, solution stability, transparency, and homogeneity were

considered primary indicators of system suitability rather than absolute pH values. DEA was employed as a complexing and stabilizing agent to regulate hydrolysis and condensation reactions of Zn precursors. The addition of DEA yielded a transparent and homogeneous solution corresponding to a nominal pH range of approximately 8–9, consistent with colloidal stabilization principles. DEA-modified sol–gel system was considered electrokinetically suitable for EPD, as the stabilized Zn-complex species promote controlled migration and deposition under an applied electric field. The solution was stirred in a beaker at 60°C for 1 hour. The solution was aged by being cooled and then left to stand at room temperature for one day.

After deposition, the coated samples were gently removed from the suspension and dried at room temperature to allow solvent evaporation. Subsequently, the coatings were heat-treated at 600 °C for 1 h in air with a heating rate of 1 °C/min to improve crystallinity and remove residual organic species.The same deposition and heat treatment parameters were applied to both coating routes to isolate the influence of suspension chemistry.

The phase composition and crystallographic structure of the coatings were analyzed by X-ray diffraction (XRD) using an X-ray diffractometer equipped with Cu Kα radiation (λ = 1.5406 Å). The measurements were conducted in the 2θ range of 20°–100° with a scanning step size of 0.02°.

Diffraction peaks were identified using standard reference data (JCPDS database). Crystallite size was estimated using the Scherrer equation:

$$D = (K\lambda) / (\beta \cos\theta) \quad (1)$$

where D is the crystallite size, K is the shape factor (typically 0.9), λ is the X-ray wavelength, β is the full width at half maximum (FWHM) of the selected diffraction peak and θ is the Bragg angle. Comparative evaluation of peak intensity, peak broadening and preferred orientation was performed to assess the influence of deposition route on crystallographic evolution.

SEM observations were carried out under high-vacuum conditions at an accelerating voltage of 5–20 kV. Secondary electron (SE) imaging mode was employed to evaluate surface topography and coating morphology. Micrographs were acquired at magnifications of 500×, 2000× and 5000× in order to systematically assess coating uniformity, particle packing behavior, surface porosity, crack formation and interfacial adhesion characteristics. For cross-sectional observations, coated samples were embedded in epoxy resin and polished to reveal the coating–substrate interface. The coating thickness was measured from multiple locations to determine deposition consistency. Elemental composition and spatial distribution were analyzed using an energy-dispersive X-ray spectroscopy (EDS) detector integrated into the SEM system.

To evaluate the porosity of ZnO surfaces, digital image analysis was carried out using ImageJ software. The top view of the ZnO surfaces was scanned using SEM at 5000x magnification, and the images were converted to 8-bit grayscale images. Otsu's thresholding technique was applied to differentiate the porous areas and microcracks from the ZnO matrix based on grayscale level differences. The porosity percentage was found as the ratio of the pore-occupied area to the total surface area of the ZnO surfaces.

The electrical resistance of WAAM-fabricated Inconel 625 specimens both before and after ZnO coating was measured using a Wheatstone bridge configuration under ambient laboratory conditions (25 ± 2 °C).

Electrical contacts were established using tightly fixed copper clamps positioned at identical locations for all measurements to ensure repeatability. In Wheatstone bridge circuit, two precision resistors (R_1 and R_2) were selected with equal resistance values ($R_1 = R_2$), establishing a bridge ratio of unity. Under balanced conditions, the unknown resistance (R_x) of the specimen corresponds directly to the adjustable resistance (R_3).

$$R_x = (R_2/R_1) \times R_3 \quad (2)$$

Each measurement was repeated three times and averaged. The electrical resistivity (ρ) was calculated using:

$$\rho = R_x \times (L/A) \quad (3)$$

where A, cross-sectional area (width × thickness) and L, effective distance between voltage terminals. Electrical conductivity (σ) was obtained as:

$$\sigma=1/\rho \quad (4)$$

For coated specimens, ZnO film thickness was considered negligible compared to the 1 mm substrate thickness in cross-sectional calculations; therefore, conductivity values primarily reflect bulk substrate behavior modified by surface effects.

3. EXPERIMENTAL FINDINGS

Surfaces fabricated via WAAM methods are often characterized by relatively higher surface roughness due to metal deposition in layers and overlapping beads during solidification. Values for WAAM-produced similar nickel alloy surfaces range from Ra ≈ 15-40 µm [2-3, 20, 45]. Light grinding using 400 and 800 grit SiC papers is performed on the WAAM-produced surfaces to remove loosely adhered surface irregularities and surface oxides. This is done without affecting the overall morphology of the substrate. This is a common practice for coating deposition on surfaces to improve their stability and reproducibility.

The surface morphology of the as-fabricated WAAM Inconel 625 substrate was presented in figure 1. SEM image was acquired at an accelerating voltage of 15 kV, a working distance of 10.3 mm and a magnification of 1000×. The micrograph reveals a relatively dense and continuous surface without visible macro-cracks or large-scale porosity. Parallel surface grooves are observed which are attributed to the post-processing or light grinding applied after waterjet sectioning. Importantly, the underlying WAAM-induced topographical characteristics are still discernible. The surface exhibits a moderately undulated morphology rather than a mirror-polished finish, indicating that the characteristic layer-wise deposition features of WAAM. Such surface undulations are typical for WAAM-fabricated structures due to layer-by-layer metal deposition and bead overlap [3]. Even after light grinding, micro-scale height variations remain. These features are particularly relevant for subsequent EPD, as surface asperities may locally intensify electric field lines, potentially influencing particle migration and deposition uniformity [18]. No evidence of surface melting defects, microcracks or significant oxidation scales is observed at this magnification, suggesting that the substrate provides a structurally stable base for coating deposition.

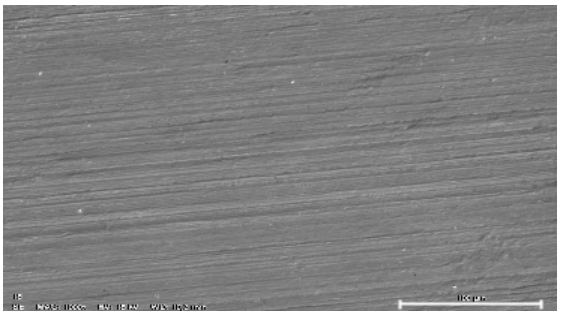

Figure 1. SEM micrograph of WAAM-fabricated Inconel 625

Figure 2a presents the elemental mapping of WAAM Inconel 625 surface while figure 2b shows the corresponding EDS spectrum. The elemental distribution confirms the presence of the principal alloying elements of Inconel 625. The elemental maps indicate a relatively homogeneous spatial distribution of Ni and Cr across the scanned region. Mo and Nb are also detected with slightly localized intensity variations which may be associated with interdendritic segregation typical of WAAM-processed nickel-based superalloys [19]. Such microsegregation is consistent with rapid solidification and repeated thermal cycling inherent to the WAAM process. Compositional fluctuations are consistent with microsegregation phenomena commonly reported in WAAM-processed Inconel 625 alloys [20]. However, at the present magnification, no distinct secondary phase particles are clearly resolved.

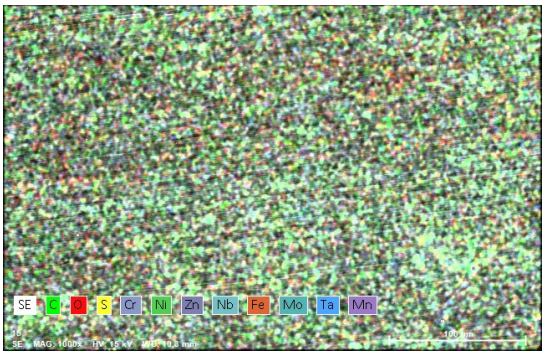

(a)

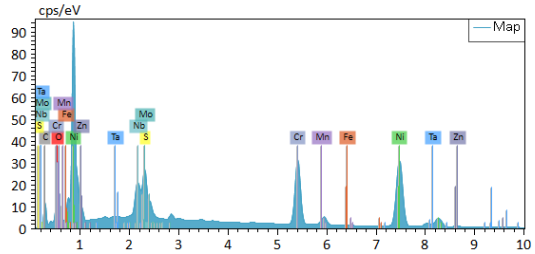

(b)

Figure 2. (a) The elemental mapping of WAAM Inconel 625 surface and (b) the corresponding EDS spectrum.

EDS spectrum further confirms the dominance of Ni, followed by Cr, Mo and Nb which aligns with the nominal composition of Inconel 625. The relative peak intensities are consistent with the expected composition range of the alloy. No unexpected impurity elements are detected at significant levels. Oxygen appears at low intensity which can be attributed to the naturally formed passive oxide layer (primarily Cr_2O_3 and NiO) that develops on nickel-based superalloys exposed to air [21]. The presence of this thin passive film is particularly relevant for subsequent coating processes. The surface oxides may have an effect on surface charge density, electrochemical potential and electrophoretic adhesion [22]. However, the low oxygen signal suggests that no thick oxide scale is present which is advantageous for ensuring good coating adhesion during EPD and may even promote interfacial bonding through surface hydroxyl groups [23]. Therefore, slight intensity variations in Nb and Mo may indicate microsegregation which could locally modify electric field distribution during EPD. The absence of heavy oxidation suggests that the waterjet cutting and light grinding did not introduce thermal damage or oxidation artifacts [24].

These features are important because they directly relate to the hypothesis that substrate heterogeneity may differently influence EPD and sol–gel derived EPD.

X-ray diffraction patterns of ZnO coatings deposited via EPD (ZnO(1)) and sol–gel derived EPD (ZnO(2)) are presented in figure 3. The diffraction patterns show characteristic peaks that are due to hexagonal wurtzite structures of ZnO with a space group of P63mc [25]. The major peaks of diffraction are clearly seen in the figure. This is in agreement with the reference data for ZnO (JCPDS 36-1451). Thus, the successful formation of ZnO is confirmed for both deposition methods. Table 2 shows XRD results of ZnO thin films.

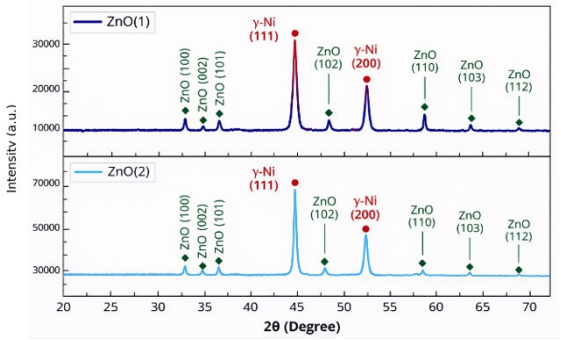

Figure 3. XRD peaks of ZnO(1) and ZnO(2) coatings

Table 2. XRD results of ZnO thin film

Sample	Peak position 2θ (°)	FWHM β (°)	Crystallite size D(nm)	Microstrain (ε) x10-3
ZnO (1)	32.060	0.74000	11.17	11.24
	34.750	1.10000	7.57	15.34
	36.470	1.10000	7.60	14.57
	47.150	1.22000	7.10	12.20
	56.870	1.58000	5.72	12.73
	63.110	0.47500	19.40	3.40
	68.270	0.75000	19.95	3.11
Sample	Peak position 2θ (°)	FWHM β (°)	Crystallite size D(nm)	Microstrain (ε) x10-3
ZnO(2)	32.010	0.84000	9.84	12.78
	34.690	0.26000	32.01	3.63
	36.410	0.84000	9.96	11.14
	47.100	0.38000	22.81	3.80
	56.810	0.72000	12.54	5.81
	63.010	0.48000	19.41	3.42
	68.230	0.48000	19.99	3.09

There were no other peaks associated with secondary phases of zinc such as $Zn(OH)_2$. A strong peak was observed at approximately 44-45°, much sharper than the ZnO peaks. This peak is associated with the (111) planes of the γ-Ni FCC matrix in the Inconel 625 alloy [26]. Nickel-based superalloys exhibit strong diffraction peaks at ~44.5° as γ-Ni (111), ~51.8° as γ-Ni (200) and ~76.4° as γ-Ni (220) [27]. The observation of these diffraction peaks shows that the ZnO coatings are thin enough to allow transmission of X-ray beams. This observation is expected for thin-film electrophoretic deposition coatings which are known to be within the micrometer to sub-micrometer range [28].

There are clear differences between the two coatings with regard to the intensity and

sharpness of the diffraction peaks. Sol-gel derived EPD coating shows much higher peak intensities and sharper diffraction peaks with minimal peak broadening. On the other hand, EPD coating (ZnO(1)) shows much lower peak intensities and broader peaks. The sharpness and intensity of the peaks are related to crystallite size and crystallinity as well as microstrain within the structure [29]. The sharpness of the peaks for sol-gel-derived coating shows much larger crystallite sizes and lower microstrain within the structure.

These differences can be explained in terms of the homogeneity of the precursors at the molecular level, as well as the hydrolysis and condensation processes which allow for in-situ nucleation during the heat treatment process [30]. On the other hand, EPD makes use of existing particles where particle stacking dominates crystal growth, unlike sol-gel derived systems where controlled crystal growth occurs [31].

For sol-gel derived EPD coating ZnO film, the intensity of the (002) reflection at 34.4° is higher than for EPD coating film which indicates a higher degree of c-axis alignment of the crystal structure perpendicularly to the substrate [32]. This higher intensity of the reflection also suggests improved crystallographic texture and vertical growth of the crystal structure which are often characteristics of sol-gel-derived systems, where controlled nucleation occurs during the sol-gel process [33]. In addition, sharper reflection peaks for sol-gel derived film suggest a lower degree of broadening of the diffraction peaks which is indicative of larger crystal sizes using Scherrer relationship [34]. These observations suggest improved crystallographic texture for sol-gel derived EPD route compared to the powder-based route.

Figure 4 shows SEM observations of ZnO coatings 500X, 2000X and 5000X, respectively.. Although no direct phase transformation at the interface was detected via XRD, the observed differences in coating compactness suggest that substrate-induced electrokinetic variations may influence particle packing behavior.

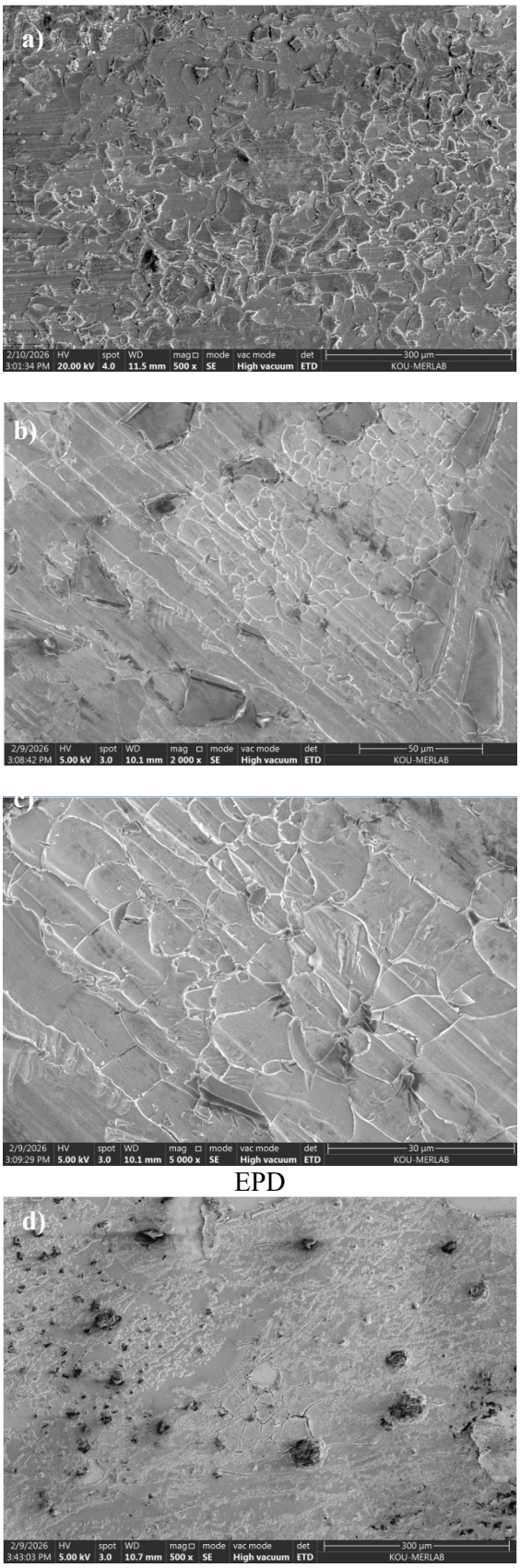

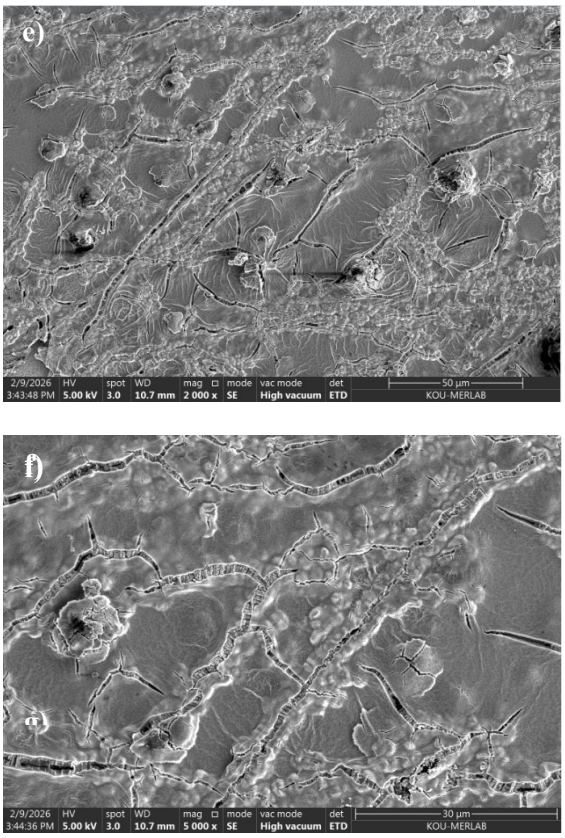

Figure 4. SEM micrographs of ZnO thin films –top view. EPD a) 500X , b) 1000X, c) 5000X, sol-gel derived EPD d)500X, e) 1000X, f) 5000X.

At low magnification, EPD coating exhibits a heterogeneous surface morphology characterized by irregular particle clusters and non-uniform surface coverage. WAAM-induced layer-wise substrate morphology remains partially visible, indicating that the coating does not fully level the underlying surface undulations [35]. Localized discontinuities and micro-void regions can be observed, suggesting incomplete packing of deposited ZnO particles. As shown by the intermediate magnification image of EPD coating, it has been found to comprise loosely arranged clusters of ZnO particles. Boundaries between particles are easily identifiable and cracks are evident along the interfaces of the clusters. The cracks may be attributed to drying and limited interparticle necking during post-deposition processing [36]. The morphology of the coating suggests the formation was influenced by particle stacking rather than condensation-induced densification. At high magnification, it has been found that the coating has a relatively rough structure with identifiable particle boundaries and porosity. The presence of microcrack networks and intergranular porosity suggests limited structural coherence. Such morphology may be responsible for the generation of electrical discontinuity and improved charge scattering at the grain boundaries [37].

On the other hand, sol–gel derived EPD coating showed a smoother surface morphology when it was viewed under low magnification. Although surface features and isolated dark areas are evident on the surface of the coating, it has been found to be relatively smoother with improved surface conformity to the substrate. At intermediate magnification, it has been found that sol–gel derived EPD coating has a relatively denser structure with fewer interparticle porosities. Boundaries between particles are relatively less distinct compared to the coating prepared by the conventional method. This may be attributed to condensation-assisted interparticle bridging during coating formation. The microcrack density has been found to be relatively lower and more confined to specific areas of the surface. At high magnification, it has been found that the surface morphology of sol–gel derived EPD coating has improved with a relatively finer structure and improved particle packing density. Such improved interconnectivity between particles may be attributed to the molecular precursor-assisted deposition and condensation mechanisms [38]. Table 3 shows crack formation mechanism for both EPD routes.

Table 3. Summary of Crack Formation Mechanisms in Powder-Based and Sol–Gel Derived EPD ZnO Coatings

Mechanistic Factor	EPD	Sol–Gel Derived EPD
Primary deposition unit	Discrete ZnO particles	Molecular/complexed Zn species
Packing mechanism	Particle stacking	Condensation-assisted network formation
Drying shrinkage behavior	Localized shrinkage at particle clusters	More homogeneous volumetric shrinkage
Interparticle bonding	Limited necking between particles	Chemical bridging during condensation
Stress distribution during drying	Stress concentration at agglomerate boundaries	More uniform stress redistribution
Crack formation tendency	Higher microcrack density and	Reduced crack density, finer microcracks

Mechanistic Factor	EPD	Sol–Gel Derived EPD
	intercluster cracks	
Porosity evolution	Interparticle void retention	Partial pore filling via precursor condensation
Expected electrical implication	Increased grain boundary scattering and local discontinuities	Improved interparticle connectivity and reduced scattering sites

EDS mapping analysis enabled visualization of dendritic and interdendritic compositional variations typical of additively manufactured nickel-based superalloys. For ZnO-coated samples, EDS mapping was further employed to confirm the presence and surface coverage of Zn and O, evaluate elemental homogeneity across the coating surface, detect potential compositional discontinuities or localized agglomeration. Due to the relatively thin nature of the deposited ZnO films, partial substrate signal contribution was considered during spectral interpretation (figure 5). Due to the thin nature of the coating and substrate signal overlap, EDS quantitative values should be considered semi-quantitative.

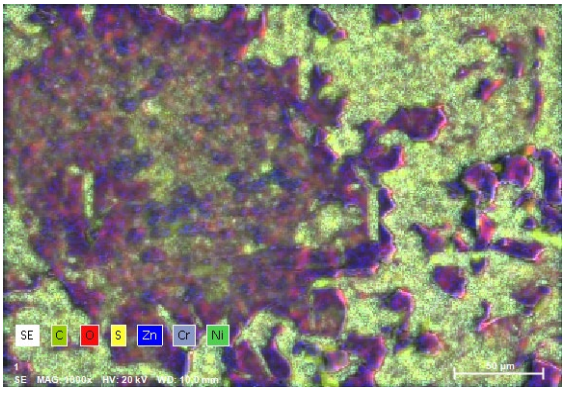

a

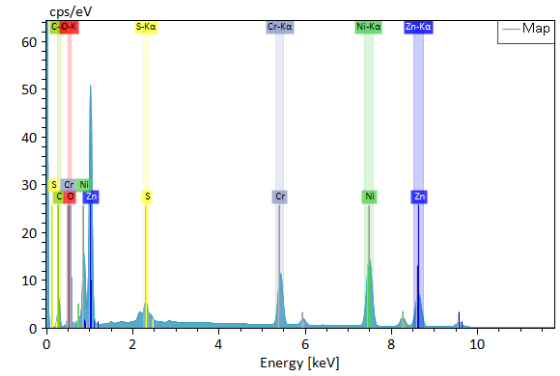

b

EPD

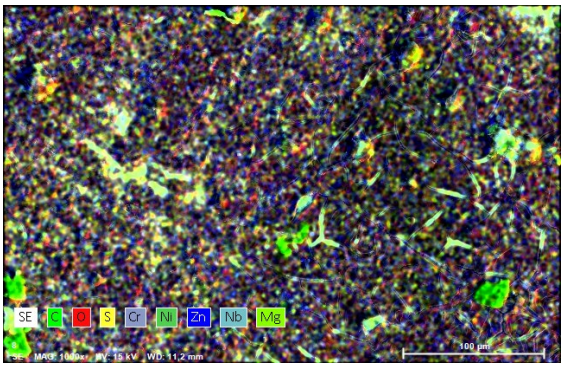

c

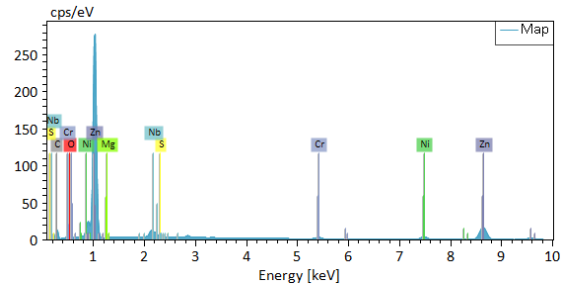

d

Sol-Gel Derived EPD

Figure 5. (a) The elemental mapping of EPD coating and (b) the corresponding EDS spectrum. (c) the elemental mapping of sol-gel derived EPD coating and (d) the corresponding EDS spectrum.

EDS spectra obtained from both coatings confirm the presence of Zn and O peaks corresponding to ZnO, together with detectable Ni and Cr signals originating from the Inconel 625 substrate. The appearance of the substrate elements in the results does not imply that the coating layer was not fully covered but rather points to the thickness of the layers deposited and the electron interaction volume associated with the EDS analysis process [15].

Quantitative results (table 4) indicate a significant difference in the composition of the two deposition routes. EPD coating layer was found to contain Ni and Cr at 28.22 wt.% and 10.85 wt.%, respectively. Zn was detected at 24.45 wt.%. Consequently, the Zn/(Ni+Cr) ratio was determined to be 0.62, indicating significant substrate contributions with minimal attenuation of the alloy substrate. On the other hand, sol-gel derived EPD coating layer was found to contain a higher Zn content of 49.91 wt.%, with Ni content being significantly reduced to 11.11 wt.% and Cr being 4.31 wt.%. Consequently, Zn/(Ni+Cr) ratio was determined to be 3.23, indicating a dominant coating contribution with a significantly reduced substrate interaction volume. Elemental

mapping supports these quantitative findings. EPD coating displays heterogeneous Zn distribution, with localized signal intensification associated with particle agglomeration regions observed in SEM micrographs. The distribution of Ni and Cr signals appears relatively continuous but with relatively less intensity, indicating inadequate substrate shielding. Conversely, sol–gel derived coating shows relatively better zinc distribution on the substrate with relatively less substrate-associated elemental signals. Quantification of the elements in the coatings using EDS technique is semi-quantitative in nature. However, Zn/(Ni+Cr) ratio is a reliable parameter that can be used to determine the efficiency of the coating process. Zn/(Ni+Cr) ratio is significantly higher in sol–gel derived EPD coating compared to EPD coating.

Table 4. Comparative Elemental Distribution and Zn/(Ni+Cr) Ratio Analysis of EPD Coatings

Element	EPD (wt.%)	Sol–Gel Derived EPD (wt.%)
Ni	28.22	11.11
Zn	24.45	49.91
C	21.38	13.27
O	13.22	18.87
Cr	10.85	4.31
Trace	1.88	2.53
Sum	100.00	100.00
Zn/(Ni+Cr)	**0.62**	**3.23**

The cross-sectional SEM study indicates that the coatings have different surface morphologies (figure 6). Sol–gel derived coating has a dense morphology with an average thickness of 0.92 ± 0.18 µm. The film is observed to have limited interfacial voids with a well-defined but coherent coating/substrate interface. The relatively smooth surface morphology indicates that the nucleation is well-controlled with homogeneous particle growth [39]. In contrast, EPD coating shows a greater thickness of 1.4 ± 0.2 µm and a more heterogeneous microstructure. The presence of loosely packed agglomerates and interparticle porosity indicates particle-stacking–dominated deposition with limited structural rearrangement [40]. Although mechanically adhered, the interface is comparatively less compact (figure 6).

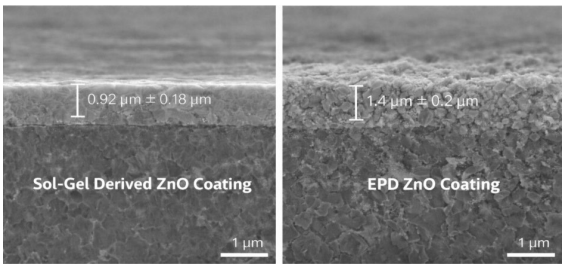

Figure 6. Cross-sectional SEM images of ZnO coating

The obtained sub-micron to ~1.5 µm thickness range is fully consistent with low-voltage (10 V) short-duration (1 min) EPD conditions. The results demonstrate that deposition chemistry governs coating densification and architecture which is expected to directly influence electrical transport behavior and interfacial charge transfer characteristics [41]. These thickness dimensions indicate a stable deposition process without excessive particle accumulation or gas-induced defects [42].

From quantitative porosity analysis, a significant variation in coating packing density was noted. Conventional EPD coating had a porosity level of 14.2% ± 1.5% which is due to random agglomeration of ZnO particles and the occurrence of shrinkage microcracks as revealed via SEM images (figure 4). However, for sol-gel derived EPD coating, a more compact coating structure is noted, with a porosity level of 3.8% ± 0.6%. This significant decrease in porosity by approximately 73% confirms that the sol-gel process favors a more continuous integration process, effectively filling interstitial space commonly encountered in conventional EPD. These results are consistent with those observed for improved electrical stability which was mentioned in following section.

Electrical resistance measurements of uncoated and ZnO-coated WAAM-fabricated Inconel 625 specimens are summarized in table 5. All measurements were performed at room temperature under identical contact conditions to ensure comparability.

Table 5. Electrical properties of uncoated and ZnO-coated WAAM Inconel 625

Sample Condition	Measured Resistance (R_x) [Ω]	Electrical Resistivity (ρ) [Ω·m]	Electrical Conductivity (σ) [S/m]	Conductivity Change (%)
Uncoated Inconel 625	6.45×10^{-6}	1.29×10^{-6}	7.75×10^{5}	Reference
ZnO EPD	7.20×10^{-6}	1.44×10^{-6}	6.94×10^{5}	↓ ~10.5%
ZnO Sol–Gel Derived EPD	6.95×10^{-6}	1.39×10^{-6}	7.19×10^{5}	↓ ~7.2%

Uncoated WAAM Inconel 625 specimen was found to have a resistivity of 1.29 x 10^{-6} Ω·m which was within the range of reported values for this alloy under ambient conditions [43]. Following the deposition of ZnO coatings using both routes of EPD, it was found that there was a measurable change in the electrical conductivity of the material. This change was found to be mainly due to the semiconducting nature of ZnO and the surface resistivity of the material. The change in electrical conductivity of Inconel 625 was found to be due to the additional resistivity elements resulting from the surface phenomena. Since ZnO is a semiconductor material with a wide bandgap of 3.37 eV and Inconel 625 is a metallic alloy with high electrical conductivity, the deposition of coating inherently results in the formation of a metal-semiconductor junction and may be considered as partially Schottky-like in nature [44].

WAAM-fabricated Inconel 625 surfaces are known to contain heterogeneous passive oxide regions enriched in NiO and Cr_2O_3 which can further modify interfacial electronic structure and promote localized barrier formation [45]. As a consequence, partial electron reflection, enhanced carrier scattering and increased contact resistance are expected at the metal/ZnO boundary. These interfacial effects contribute to the approximately 7–11% reduction in electrical conductivity observed after coating.

SEM observation provided additional insight into the electrical response. EPD coating exhibits microcrack networks and heterogeneous particle stacking, features that can introduce discontinuities in electron transport pathways and increase grain boundary scattering. In contrast, sol–gel derived EPD coating presents improved surface continuity, reduced crack density and more homogeneous particle distribution, suggesting enhanced interparticle connectivity and more uniform interfacial bonding [40]. These morphological differences are consistent with the slightly lower conductivity reduction measured for sol–gel route compared to the conventional.

Nevertheless, the overall electrical characteristics are still dominated by the substrate due to the negligible thickness of the ZnO film (~1 μm) in comparison with that of thick metallic substrate. The system can therefore be modeled in terms of a series resistance model, in which the total resistance is a combination of metallic, interfacial and film resistances. The small decrease in conductivity is physically understandable in terms of a thin layer of semiconductor material rather than a system in which conduction is dominated by the thin film. The results show that the chemistry of suspension is seen to have an effect not only on compactness but also on interfacial charge transport characteristics, with sol-gel derived EPD process yielding enhanced interfacial coherence and reduced resistive disruption.

The differences found with regard to the distribution of elements and the contribution of the substrate signal offer further insight into the electrical results. Since it has been verified via EDS that the coatings are still of sufficient thickness to allow for the contribution of the substrate within the interaction volume, it may be expected that the overall electrical results will be dominated by the substrate [46]. However, sol–gel-derived EPD coating has been found to have a relatively higher Zn/(Ni+Cr) ratio and improved compactness which are signs of fewer localized discontinuities and improved interfacial contact. Such structural coherence would be expected to reduce excessive interfacial resistive effects and would explain the relatively smaller change found for sol–gel derived EPD coating.

Comparative analysis reveals the pivotal role of the morphological architecture with regard to electrical transport phenomena. The morphology of EPD coatings tends to be more porous and agglomerated. This leads to an increase in the density of grain boundaries and interparticle contact resistances. Such features

are capable of generating potential barriers and may act as electron scattering sites [47]. This limits the mobility of the charge carriers. On the other hand, sol–gel derived EPD coatings are found to be more dense and have better continuity. This reduces the intergranular porosity and facilitates better electron mobility [48]. The lower density of defects and better interconnection of particles are expected to reduce the scattering of the charge carriers and improve electrical stability.

ZnO porous architectures may offer advantages for applications where surface area is crucial, such as gas sensors and optoelectronic devices where adsorption-controlled mechanisms play a major role [49]. In these cases, surface activity may be more beneficial than the disadvantages related to low electron mobility. Therefore, the morphology will be application-dependent.

Collectively, the structural, morphological and electrical analyses suggest that sol-gel derived electrophoretic deposition route enables improved crystallographic orderliness and compactness of the film, which in turn enables a comparatively lower resistive effect and more stable charge transport characteristics for the WAAM-fabricated Inconel 625 substrates.

4. RESULTS

In this study, ZnO coatings were successfully deposited on WAAM-fabricated Inconel 625 substrates using powder-based and sol–gel derived electrophoretic deposition routes. Both methods produced crystalline ZnO coatings consistent with wurtzite phase as confirmed via XRD analysis; however, the sol–gel derived route resulted in improved crystallinity, enhanced (002) preferential orientation and a more compact morphology. SEM and EDS analyses revealed that powder-based coatings exhibited microcracks and heterogeneous particle stacking, whereas sol–gel derived coatings provided more uniform surface coverage and reduced defect density. Electrical measurements indicated a moderate decrease in conductivity (≈7–11%) after coating, attributed to metal–semiconductor interfacial effects. Compared to the powder-based route, the sol–gel derived coatings showed a smaller conductivity reduction, suggesting improved interfacial coherence and charge transport stability. The results demonstrate that suspension chemistry significantly influences coating structure and electrical behavior on WAAM-fabricated Inconel 625 and sol–gel derived EPD offering improved structural integrity and electrical performance.

ACKNOWLEDGES

This work has been supported by Tubitak project number 1002-A 225M007.

REFERENCES

1. Kishor, G., Mugada, K.K., Mahto, R.P., “Wire arc additive manufacturing of titanium alloys for enhancing mechanical properties and grain-refinement”, Metals and Materials International, Vol. 32, Issue 1, Pages 50-80, 2026.

2.Bhuvanesh Kumar, M., Sathiya, P., Senthil, S.M., “A critical review of wire arc additive manufacturing of nickel-based alloys: principles, process parameters, microstructure, mechanical properties, heat treatment effects, and defects”, Journal of the Brazilian Society of Mechanical Sciences and Engineering, Vol. 45, Issue 3, Pages 164, 2023.

3.Iqbal, H., Ascari, A., Fortunato, A., Liverani, E., “Elucidating the effects of metal transfer modes and investigating the material properties in wire-arc additive manufacturing (WAAM)”, Progress in Additive Manufacturing, Vol. 10, Issue 5, Pages 3335-3360, 2025.

4.Saeed, M., Marwani, H.M., Shahzad, U., Asiri, A.M., Rahman, M.M., “Recent advances, challenges, and future perspectives of ZnO nanostructure materials towards energy applications”, The Chemical Record, Vol. 24, Issue 1, Pages e202300106, 2024.

5.Zhan, F., Wen, G., Li, R., Feng, C., Liu, Y., Liu, Y., La, P., “A comprehensive review of oxygen vacancy modified photocatalysts: synthesis, characterization, and applications”, Physical Chemistry Chemical Physics, Vol. 26, Issue 15, Pages 11182-11207, 2024.

6.Abdullah, M.T., Sherzad Othman, M., “Analysing magnesium oxide nanostructures prepared using several methods: a review”, Physica Scripta, Vol. 100, Issue 12, Pages 122001, 2025.

7.Chakrabarti, B.K., Gençten, M., Bree, G., Dao, A.H., Mandler, D., Low, C.T.J., “Modern practices in electrophoretic deposition to manufacture energy storage electrodes”, International Journal of Energy Research, Vol. 46, Issue 10, Pages 13205-13250, 2022.

8.Wang, Y., Yang, Y., Liu, M., "Electrophoretic deposition of halloysite nanotubes/PVA composite coatings for corrosion protection of metals", Applied Materials Today, Vol. 29, Pages 101657, 2022.

9.Kou, Q., Ge, C., Sun, L., Qi, W., Xu, J., Zhang, J., Ye, H., "Preparation of TiB2 coatings on graphite via electrophoretic deposition in NaCl-KCl-AlF3 molten salts", Journal of The Electrochemical Society, Vol. 172, Issue 1, Pages 012503, 2025.

10.Sikkema, R., Zhang, C., Zhitomirsky, I., "New developments in synthesis of bioceramics, electrophoretic deposition of biopolymer, and composites using organic bases", Colloids and Surfaces A: Physicochemical and Engineering Aspects, Vol. 716, Pages 136691, 2025.

11.Azzouz, I., Khlifi, K., Faure, J., Dhiflaoui, H., Larbi, A.B.C., Benhayoune, H., "Mechanical behavior and corrosion resistance of sol-gel derived 45S5 bioactive glass coating on Ti6Al4V synthesized by electrophoretic deposition", Journal of the Mechanical Behavior of Biomedical Materials, Vol. 134, Pages 105352, 2022.

12.Yu, Y., Matsunaga, M., "Sol–Gel Electrophoretically Deposited TiO2–Multiwalled Carbon Nanotube–SiO2 Thin-Film Electrode with High Photoelectrochemical Activity", ACS Omega, Vol. 10, Issue 8, Pages 7857-7875, 2025.

13.Sharma, G., Rathore, S., Kumar, H., Yadav, K.K., "Wear Properties of Wire and Arc Additive Manufacturing Components: A review on recent developments on Processes, Materials and Parameters", Library of Progress-Library Science, Information Technology & Computer, Vol. 44, Issue 3, 2024.

14.Hashish, M., "Abrasive waterjet machining", Materials, Vol. 17, Issue 13, Pages 3273, 2024.

15.Verde, M., Peiteado, M., Caballero, A.C., Villegas, M., Ferrari, B., "Electrophoretic deposition of transparent ZnO thin films from highly stabilized colloidal suspensions", Journal of Colloid and Interface Science, Vol. 373, Issue 1, Pages 27-33, 2012.

16.Han, Y., Hwang, G., Kim, D., Bradford, S.A., Lee, B., Eom, I., Kim, H., "Transport, retention, and long-term release behavior of ZnO nanoparticle aggregates in saturated quartz sand: Role of solution pH and biofilm coating", Water Research, Vol. 90, Pages 247-257, 2016.

17.Chang, C., Rad, S., Gan, L., Li, Z., Dai, J., Shahab, A., "Review of the sol–gel method in preparing nano TiO2 for advanced oxidation process", Nanotechnology Reviews, Vol. 12, Issue 1, Pages 20230150, 2023.

18.Zhao, J., Liu, W., Azari, R., Chen, L., Wang, K., Boccaccini, A.R., Sun, X.W., "Electrophoretic deposition", Nature Reviews Methods Primers, Vol. 6, Issue 1, Pages 12, 2026.

19.Feng, J., Zhang, X., Chu, Y., Wan, J., "Hydrogen embrittlement of Ni-based superalloy inconel 625 fabricated by wire arc additive manufacturing: the role of laves phase", Metals and Materials International, Vol 30, Issue 4, Pages 872-885, 2024.

20.Nandi, S., Manivannan, R., Dubey, P., Bhagyaraj, J., Chowdhury, S.G., Rajinikanth, V., "Role of inter-pass temperature on cooling rate, segregation and mechanical properties of wire arc additively manufactured Inconel 625", Materials Characterization, Pages 115869, 2025.

21.Zhang, P.Z., Tang, B., "Mechanism of high temperature oxidation of Inconel 625 superalloy with various solution and ageing heat treatment processes", Transactions of Nonferrous Metals Society of China, Vol. 34, Issue 11, Pages 3662-3676, 2024.

22.Hur, J., Choi, Y.M., Kim, T., Yi, S.H., Li, L., Chun, S.E., "Effect of applied potential polarity on electrochemical properties of electrophoretically deposited activated carbon on an indium tin oxide substrate", Surfaces and Interfaces, Vol. 37, Pages 102660, 2023.

23.Parthasarathy, S., Madhuri, A., Swain, B.P., "Adhesion and Surface Modification of Coating Materials", Advances in Mechanical Coating: Processing, Properties and Applications, Pages 109-136, Springer Nature Singapore, Singapore, 2025.

24.Wei, J., Yuan, S., Yang, S., Gao, M., Fu, Y., Hu, T., Zhang, W., "Waterjet-guided laser processing of SiC/SiC ceramic matrix composites to obtain high cleanliness and low oxidation damage characteristics surfaces", Surface and Coatings Technology, Vol. 484, Pages 130791, 2024.

25.Mohammada, A., Al-Jafa, H.A., Ahmeda, H.S., Mohammedb, M., Khodairc, Z., "Structural and morphological studies of ZnO nanostructures", Journal of Ovonic Research, Vol. 18, Issue 3, Pages 443-452, 2022.

26.Mahendiran, S., Ramanujam, R., "Investigation of surface residual stress, mechanical properties, and metallurgical characterization of Inconel 625 multilayer thin-wall component using cold metal transfer technique", Journal of Materials Engineering and Performance, Vol. 34, Issue 2, Pages 1026-1049, 2025.

27.Madesh, R., Kumar, K.G., "Development of metallurgical and mechanical properties of nickel-based superalloy employed by wire arc additive manufacturing technique", Journal of Materials Engineering and Performance, Vol. 33, Issue 13, Pages 6718-6737, 2024.

28.Kumar, A., Jaiswal, J., Tsuchiya, K., Mulik, R.S., "Modern coating processes and technologies", Coating Materials: Computational Aspects, Applications and Challenges, Pages 33-80, Springer Nature Singapore, Singapore, 2023.

29.Samanta, P.K., "Effect of microstrain on the crystallite size of ZnO nanoparticles: X-ray peak profile and Rietveld analysis", Next Materials, Vol. 8, Pages 100841, 2025.

30.Srilatha, N., Prasad, S.S., Sahithi, V.V.D., Hari, S.S., Balashowry, K., "Developing Hybrid and Functional Materials with Sol-gel Chemistry–A Review", Journal of Environmental Nanotechnology, Vol. 14, Issue 3, Pages 540-558, 2025.

31.Karmakar, S., Deo, M., Rahaman, I., Mohanty, S.K., "Nanoparticle Deposition Techniques for Silica Nanoparticles: Synthesis, Electrophoretic Deposition, and Optimization-A review", arXiv preprint, arXiv:2503.22593, 2025.

32.Nizar, B.M., Lajnef, M., Chaste, J., Chtourou, R., Herth, E., "Highly C-oriented (002) plane ZnO nanowires synthesis", RSC Advances, Vol. 13, Issue 22, Pages 15077-15085, 2023.

33.Bouderbala, I.Y., Guessoum, A., Rabhi, S., Bouhlassa, O., Bouras, I.E., "Optical band-diagram, Urbach energy tails associated with photoluminescence emission in defected ZnO thin films deposited by sol–gel process dip-coating: effect of precursor concentration", Applied Physics A, Vol. 130, Issue 3, Pages 205, 2024.

34.Khorsand Zak, A., Hashim, A.M., "Advanced XRD peak broadening analysis of gallium-doped ZnO nanoparticles for crystallite size evaluation", Scientific Reports, 2025.

35.Koul, P., Siddaramu, Y., "A Review of Wire Arc Additive Manufacturing", International Journal of Scientific Research in Modern Science and Technology, Vol. 4, Issue 8, Pages 01-32, 2025.

36.De Riccardis, M.F., "Ceramic coatings obtained by electrophoretic deposition: fundamentals, models, post-deposition processes and applications", Ceramic Coatings: Applications in Engineering, Pages 43-68, 2012.

37.Agnihotri, P., Rani, R., Bdikin, I., Sharma, S., Rai, R., "Preparation of nano-structured barium titanate via electrophoretic deposition (EPD) and their electrical and ionic conductivity via impedance spectroscopy", Ionics, Vol. 31, Issue 2, Pages 2259-2275, 2025.

38.Tasis, D., "Recent progress on the synthesis of graphene-based nanostructures as counter electrodes in DSSCs based on iodine/iodide electrolytes", Catalysts, Vol. 7, Issue 8, Pages 234, 2017.

39.Sreekala, A.P., Nair, P.R., Kadavath, J.K., Krishnan, B., Avellaneda, D.A., Anantharaman, M.R., Shaji, S., "Laser processing in liquids: insights into nanocolloid generation and thin film integration for energy, photonic, and sensing applications", Beilstein Journal of Nanotechnology, Vol. 16, Issue 1, Pages 1428-1498, 2025.

40.Karrari, S., Mohammadzadeh, H., Jafari, R., "Effect of coating parameters on the properties of the Zn–Cu–Ni oxide nanocomposite coating deposited on stainless steel 316LC by EPD", Reaction Chemistry & Engineering, Vol. 10, Issue 11, Pages 2571-2587, 2025.

41.Arun, A.P., Sreenivasan, N., Patil, J.H., Kusanur, R., Ramachandraiah, H.L., Ramakrishna, M., "Thin Films for Next Generation Technologies: A Comprehensive Review of Fundamentals, Growth, Deposition Strategies, Applications, and Emerging Frontiers", Processes, Vol. 13, Issue 12, Pages 3846, 2025.

42.Hofmann, J., Teutenberg, D., Meschut, G., "Method development for the mechanical characterisation of cathodic electrodeposition coatings for numerical simulation of bonded joints", The Journal of Adhesion, Pages 1-16, 2026.

43.Kaschnitz, E., Kaschnitz, L., Heugenhauser, S., "Electrical resistivity measured by millisecond pulse heating in comparison with thermal conductivity of the superalloy Inconel 625 at elevated temperature", International Journal of Thermophysics, Vol. 40, Issue 3, Pages 27, 2019.

44.Tun, H.M., Wulansari, R.E., Pradhan, D., Naing, Z.M., "Design, fabrication and measurement of metal-semiconductor field effect transistor based on zinc oxide material", Journal of Engineering Researcher and Lecturer, Vol. 2, Issue 3, Pages 104-111, 2023.

45.Jadhav, S., Kusekar, S., Belure, A., Digole, S., Mali, A., Cheepu, M., Kim, D., "Recent progress and scientific challenges in wire-arc additive manufacturing of metallic multi-material structures", Journal of Manufacturing and Materials Processing, Vol. 9, Issue 8, Pages 284, 2025.

46.Gartner, M., Stroescu, H., Mitrea, D., Nicolescu, M., "Various applications of ZnO thin films obtained by chemical routes in the last decade", Molecules, Vol. 28, Issue 12, Pages 4674, 2023.

47.Shah, V., Choudhury, A., Thakrar, Y., Patil, T., Dharaskar, S., "Functionalized Nanomaterial–Based Thin-Film Transistors and Display Devices", Functionalized Nanomaterials for Electronic and Optoelectronic Devices: Design, Fabrications and Applications, Pages 195-234, 2025.

48.Nunes, V.F., Júnior, P.H.F.M., Almeida, A.F.L., Freire, F.N.A., "EPD method for thin films on solar cells", Materials Letters, Vol. 358, Pages 135896, 2024.

49.Khudiar, S.S., Nayef, U.M., Mutlak, F.A.H., Abdulridha, S.K., "Characterization of NO2 gas sensing for ZnO nanostructure grown hydrothermally on porous silicon", Optik, Vol. 249, Pages 168300, 2022.